Journal of Colloid and Interface Science 608 (2022) 1116–1125

Contents lists available at ScienceDirect

Journal of Colloid and Interface Science

journal homepage: www.elsevier.com/locate/jcis

# Suppressing photoinduced charge recombination at the $BiVO_4$||NiOOH junction by sandwiching an oxygen vacancy layer for efficient photoelectrochemical water oxidation

Yong Peng [a,b], Minshu Du [c], Xingli Zou [d,*], Guohua Jia [e], Shella Permatasari Santoso [f,*], Xiang Peng [i], Wenxin Niu [g], Mingjian Yuan [h], Hsien-Yi Hsu [a,b,*]

[a] School of Energy and Environment, Department of Materials Science and Engineering, City University of Hong Kong, Kowloon Tong, Hong Kong, China
[b] Shenzhen Research Institute of City University of Hong Kong, Shenzhen 518057, China
[c] School of Materials Science and Engineering, Northwestern Polytechnical University, Xi'an, Shaanxi 710072, China
[d] State Key Laboratory of Advanced Special Steel & School of Materials Science and Engineering, Shanghai University, Shanghai 200072, PR China
[e] Curtin Institute of Functional Molecules and Interfaces School of Molecular and Life Sciences, Curtin University GPO Box U1987, Perth, WA 6845, Australia
[f] Department of Chemical Engineering, Faculty of Engineering, Widya Mandala Surabaya Catholic University, Kalijudan No. 37, Surabaya 60114, East Java, Indonesia
[g] State Key Laboratory of Electroanalytical Chemistry Changchun Institute of Applied Chemistry, Chinese Academy of Sciences 5625 Renmin Street, Changchun, Jilin 130022, PR China
[h] Key Laboratory of Advanced Energy Materials Chemistry (Ministry of Education), Renewable Energy Conversion and Storage Center (RECAST), College of Chemistry, Nankai University, Tianjin, PR China
[i] Hubei Key Laboratory of Plasma Chemistry and Advanced Materials, School of Materials Science and Engineering, Wuhan Institute of Technology, Wuhan 430205, PR China

## GRAPHICAL ABSTRACT

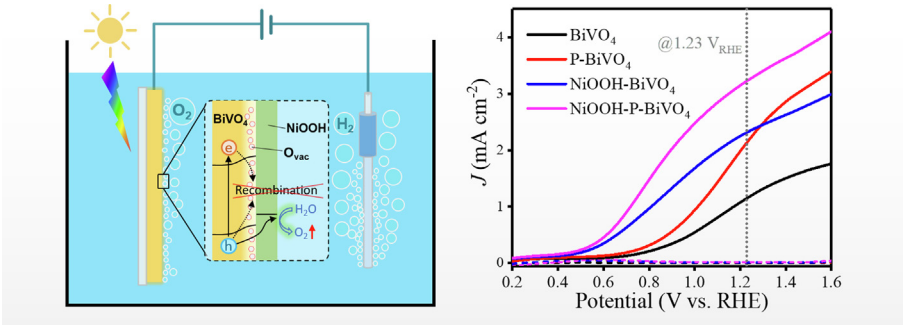


## ARTICLE INFO

*Article history:*
Received 29 July 2021
Revised 11 October 2021
Accepted 12 October 2021
Available online 23 October 2021

*Keywords:*
Photoelectrochemistry
Surface engineering
Oxygen vacancies

## ABSTRACT

Nickel oxyhydroxide (NiOOH) is regarded as one of the promising cocatalysts to enhance the catalytic performance of photoanodes but suffers from serious interfacial charge-carrier recombination at the photoanode||NiOOH interface. In this work, surface-engineered $BiVO_4$ photoanodes are fabricated by sandwiching an oxygen vacancy ($O_{vac}$) interlayer between $BiVO_4$ and NiOOH. The surface $O_{vac}$ interlayer is introduced on $BiVO_4$ by a chemical reduction treatment using a mild reducing agent, sodium hypophosphite. The induced $O_{vac}$ can alleviate the interfacial charge-carrier recombination at the BiVO4||NiOOH junction, resulting in efficient charge separation and transfer efficiencies, while an outer NiOOH layer is coated to prevent the $O_{vac}$ layer from degradation. As a result, the as-prepared NiOOH-P-$BiVO_4$ photoanode exhibits a high photocurrent density of 3.2 mA $cm^{-2}$ at 1.23 V vs. RHE under the irradiation

* Corresponding authors at: School of Energy and Environment, Department of Materials Science and Engineering, City University of Hong Kong, Kowloon Tong, Hong Kong, China (H. Hsu); State Key Laboratory of Advanced Special Steel & School of Materials Science and Engineering, Shanghai University, Shanghai 200072, PR China (X. Zou); Department of Chemical Engineering, Faculty of Engineering, Widya Mandala Surabaya Catholic University, Kalijudan No. 37, Surabaya 60114, East Java, Indonesia (S.P. Santoso).
*E-mail address:* sam.hyhsu@cityu.edu.hk (H.-Y. Hsu).

https://doi.org/10.1016/j.jcis.2021.10.063

Nickel oxyhydroxide

of 100 mW/cm$^2$ AM 1.5G simulated sunlight, in comparison to those of bare $BiVO_4$, P-$BiVO_4$, and NiOOH-$BiVO_4$ photoanodes (1.1, 2.1 and 2.3 mA cm$^{-2}$, respectively). In addition to the superior photoactivity, the 5-h amperometric measurements illustrate improved stability of the surface-engineered NiOOH-P-$BiVO_4$ photoanode. Our work showcases the feasibility of combining cocatalysts with $O_{vac}$, for improved photoactivity and stability of photoelectrodes.



## 1. Introduction

Bismuth vanadate ($BiVO_4$) is one of the potential candidates for photoelectrochemical (PEC) water splitting to produce hydrogen fuel in the future. The photoanode is endowed with a suitable bandgap structure (the bandgap of 2.4 eV and conduction band edge of 0.02 V vs. RHE for hydrogen production) and moderate charge carrier lifetime [1]. Despite this, unacceptable charge carrier recombination and poor water oxidation kinetics have significantly impaired the PEC performance of this photoanode [2]. To tackle the issue, versatile strategies including doping engineering [3], morphology engineering [4], heterostructure engineering [5], and surface modification of oxygen evolution catalysts (OECs) [6], have been employed to promote the PEC performance of $BiVO_4$ photoanodes.

In general, the overlayer of OECs has been recognized as a useful strategy to accelerate water oxidation reaction and alleviate bulk electron-hole pair recombination. Numerous OECs such as metal phosphates (e.g., CoPi) [7], metal phosphides (CoP) [8], metal oxides ($IrO_2$ and $CoO_x$) [9], and metal (oxy)hydroxides ($Ni(OH)_2$ and NiOOH) [9c,10], have been designed for improving the photoactivity of $BiVO_4$ photoelectrodes. Among these catalysts, metal oxyhydroxides such as iron oxyhydroxide (FeOOH) and nickel oxyhydroxide (NiOOH) have gained much attention because of their prominent catalytic activity, earth abundance, and environmental friendliness [11]. Notably, the modification of NiOOH as an OEC on $BiVO_4$ photoanodes enables a lower onset potential in comparison to FeOOH, which indicates an exceedingly active water oxidation process [6a]. Despite these benefits, considerable interfacial recombination of electron-hole pairs at the $BiVO_4$||NiOOH interface has significantly jeopardized its photoactivity [6a], which raises concerns about applying NiOOH for practical uses.

To eliminate interfacial charge carrier recombination, introducing an oxygen vacancies ($O_{vac}$) layer between the $BiVO_4$ photoanode and the NiOOH overlayer may be one of the effective strategies [12]. This is because $O_{vac}$ has the opportunity to modify the electronic structure and create inter-band states in the forbidden band of $BiVO_4$, resulting in both enhanced conductivity and promoted charge separation [12–13]. In the meantime, the overlaid cocatalysts may also serve as a protective layer, preventing the degradation of the $O_{vac}$ layer which is not stable in a highly oxidizing environment [12]. In view of these aspects, we propose that interfacial charge recombination may be suppressed with a rational sandwiched $O_{vac}$ layer between $BiVO_4$ photoanodes and NiOOH cocatalysts.

Herein, an interfacial $O_{vac}$ layer has been introduced to $BiVO_4$ photoanodes by a chemical reduction treatment using a mild reducing agent, sodium hypophosphite. The induced $O_{vac}$ interlayer can decrease interfacial charge carrier recombination, as indicated by the charge separation and transfer efficiencies, while the outer NiOOH layer as active sites for the oxidation of water is loaded to simultaneously prevent the $O_{vac}$ interlayer from degradation. As a result of the alleviation of the interfacial carrier recombination and the acceleration of water oxidation reaction, the PEC performance of $BiVO_4$ photoanodes can be considerably enhanced. In this work, we provide an effective and facile strategy to coordinate OECs and $O_{vac}$, leading to an improved photoactivity of metal oxide semiconductors.

## 2. Materials and methods

### 2.1. Fabrication of $BiVO_4$, P-$BiVO_4$, NiOOH-$BiVO_4$ and NiOOH-P-$BiVO_4$ films

Bare $BiVO_4$ films on FTO glass (6–9 Ω/sq) were synthesized using a reported electrodeposition method followed by the calcination [6a,14]. The pH of 50 mL DI water was adjusted to 1.7 using 65% $HNO_3$. Next, 3.32 g of KI and 0.97 g of $Bi(NO_3)_3{\cdot}5H_2O$ were subsequently added and dissolved in the aqueous solution. The as-prepared solution was mixed with 20 mL of 0.23 M *p*-benzoquinone dissolved in ethanol, which was then used as an electrolyte. FTO substrates (1.5 cm × 3.0 cm) were cleaned by sonicating them in acetone, ethanol, and DI water, each for 20 min. The cathodic deposition was then performed using a three-electrode system including the FTO glass as a working electrode, a Pt wire as the counter electrode, and an Ag/AgCl (3 M) as the reference electrode. During amperometric deposition, the potential was set at −0.1 V vs. Ag/AgCl, and each electrodeposition lasted for 5 min to achieve a total charge of around 0.13C cm$^{-2}$. The obtained BiOI films were calcined with 300 μL of 0.2 M $VO(acac)_2$ in DMSO at 450 °C for 2 h. The as-obtained $BiVO_4$ films were treated in 1 M NaOH for 30 min to remove $V_2O_5$.

To induce $O_{vac}$ into $BiVO_4$, the bare $BiVO_4$ photoanodes were placed into 0.5 M sodium hypophosphite ($Na_2H_2PO_2{\cdot}H_2O$) and heated at 90 °C for 6 h in an oven. After the treatment, the as-obtained hypophosphite-treated $BiVO_4$ (labeled as P-$BiVO_4$) was rinsed with DI water and dried with compressed air. The optimization processes for the concentration of hypophosphite, heating temperature, and duration are shown in Figure S1 (Supplementary Information, SI). To facilitate charge transfer, the NiOOH cocatalyst layer was deposited on the $BiVO_4$ and P-$BiVO_4$ photoanodes using a pH-adjusting method [15]. Specifically, after immersing the photoanodes into 10 mM $Ni(NO_3)_2{\cdot}6H_2O$ for 15 min, the pH of the solution was adjusted to be around 8.0 using 2 M NaOH. After that, the solution was remained still for 45 min to deposit NiOOH on the photoanodes. Finally, the obtained NiOOH-coated photoanodes (named NiOOH-$BiVO_4$ and NiOOH-P-$BiVO_4$, respectively) were identically rinsed and dried.

### 2.2. Material characterizations

The surface morphology was observed by Zeiss EVO MA10 scanning electron microscope (SEM) and FEI Tecnai F20 field-emission transmission electron microscope (TEM). The elemental mapping was collected by the FEI Tecnai F20 equipped with an energy-dispersive X-ray spectroscope (EDS) under STEM mode. X-ray diffraction (XRD) patterns were measured with PANalytical X'Pert3 X-ray diffractometer. X-ray photoelectron spectroscopy (XPS) was performed by the Thermo Scientific K-Alpha$^+$ XPS spectrometer. All binding energies were calibrated with respect to C 1 s peak at 284.8 eV. Electron paramagnetic resonance (EPR) spectra were measured with a Bruker A300 spectrometer. Raman spectra were

collected by a HORIBA iHR320 Raman microscope with a 514-nm laser. UV–visible absorption spectra were measured using Shimadzu UV-3600 spectrophotometer with an integrated sphere. Photoluminescence (PL) spectra were analyzed using Shimadzu RF-5301PC spectrometer. Time-resolved photoluminescence (TRPL) spectra were measured by the PicoQuant Fluo Time 200 spectrometer coupled with a TimeHarp 260 time-correlated single-photon counting (TCSPC) system.

### 2.3. Electrochemical and photoelectrochemical characterizations

A three-electrode system was used for electrochemical and photoelectrochemical measurements using a CHI660 workstation (Chenhua, Shanghai). The as-obtained films were used as working electrodes, while the counter electrode and the reference electrode were Pt wire and Ag/AgCl (3 M), respectively. The photoanodes were back-side illuminated by a 300 W xenon lamp equipped with an AM 1.5G filter and the optical power was calibrated to 100 mW $cm^{-2}$. A 0.5 M $Na_2SO_4$ aqueous solution (pH 6.6) was used as the electrolyte during the measurements. The potential versus Ag/AgCl was converted to potential versus reversible hydrogen electrode (RHE) based on the following equation:

$$E_{RHE} = E^{\ominus}_{Ag/AgCl} + E_{Ag/AgCl} + 0.059 \times pH$$

where $E_{RHE}$ is the converted potential versus RHE, $E^{\ominus}_{Ag/AgCl}$ is the standard electrode potential of Ag/AgCl electrode against the standard hydrogen electrode and equals to 0.210 V at 25 °C, and $E_{Ag/AgCl}$ is the experimentally measured potential versus Ag/AgCl electrode.

Linear sweep voltammetry (LSV) technique was carried out from −0.7 to 1.0 V vs. Ag/AgCl at a scan rate of 10 mV $s^{-1}$ under the dark or light condition to obtain current–potential (*J-V*) curves. Electrochemical impedance spectra (EIS) were collected at an imposed potential of 0.63 V vs. Ag/AgCl (equal to 1.23 V vs. RHE) with frequencies ranging from $10^5$ to 0.5 Hz and an amplitude voltage of 10 mV under illumination. The resultant EIS spectra were fitted using the Zview software. For transient photocurrent measurements, also called amperometric *i-t* tests, $BiVO_4$ films were imposed with a bias potential of 0.63 V vs. Ag/AgCl under chopped illumination (light 50 s/dark 50 s). For testing the stability of $BiVO_4$ films, the illumination lasts for 5 h at the same bias potential. Mott-Schottky (M−S) analysis was performed at a frequency of 1000 Hz at an amplitude of 10 mV from −0.6 V to 0.8 V vs. Ag/AgCl under dark. The charge carrier density of bare $BiVO_4$ and P-$BiVO_4$ films was analyzed according to the below equation.

$$N_d = \frac{2}{\varepsilon\varepsilon_o A^2 e} \times \left[\frac{d\left(\frac{1}{c^2}\right)}{dV}\right]^{-1}$$

where $N_d$ is donor density (in $m^{-3}$), $\varepsilon$ is relative permittivity (68 for $BiVO_4$ [16], $\varepsilon_o$ is vacuum permittivity (=8.85 × $10^{-12}$F $m^{-1}$), *A* is surface area (=2.83 × $10^{-5}$ $m^2$ in this study), *e* is electronic charge (=1.602 × $10^{-19}$C), *c* is interfacial capacitance (in F), and *V* is applied voltage (in V). The incident photon-to-current conversion efficiency (IPCE) was obtained using a Cornerstone 260 monochromator with a 300 W Xenon light source, based on the following equation.

$$IPCE(\%) = \frac{1240 \times J_{photo}}{P_{light} \times \lambda} \times 100\%$$

where $\lambda$ is the wavelength of monochromatic light (in nm), $J_{photo}$ is the photocurrent density under the light (in mA $cm^{-2}$), and $P_{light}$ is the measured irradiance of the light (in mW $cm^{-2}$).

Charge separation and charge transfer efficiencies of the photoanodes were analyzed using hole scavenger sodium sulfite ($Na_2SO_3$), assuming that the oxidation kinetics of sulfite ions by photogenerated holes is very fast and the charge transfer efficiency reaches 100% [17]. The charge separation ($\eta_{separation}$) and charge transfer ($\eta_{transfer}$) efficiencies were calculated by the following equation.

$$\eta_{separation} = \frac{J_{photo,sulfite}}{J_{absorption}} \times 100\%$$

$$\eta_{transfer} = \frac{J_{photo,water}}{J_{photo,sulfite}} \times 100\%$$

where $J_{photo,sulfite}$ is the calculated photocurrent density by subtracting current density measured in 0.5 M $Na_2SO_3$ (pH 10.6) in dark from the current density obtained under irradiation, $J_{photo,water}$ is the calculated photocurrent density measured in 0.5 M $Na_2SO_4$, and $J_{absorption}$ is theoretical cumulative photocurrent density from light absorption, derived from integrating light absorptance with respect to AM 1.5G solar spectrum.

## 3. Results and discussion

As depicted in Scheme 1, a controllable chemical treatment using sodium hypophosphite followed by coating NiOOH as cocatalysts has been employed to modify $BiVO_4$ films. The pristine $BiVO_4$ films were first treated with 0.5 M hypophosphite ($NaH_2PO_2$) aqueous solution to prepare hypophosphite-treated $BiVO_4$ (labeled as P-$BiVO_4$). Then, both $BiVO_4$ and P-$BiVO_4$ films were deposited with NiOOH cocatalysts using a pH-adjusting technique to get NiOOH--coated $BiVO_4$ (NiOOH-$BiVO_4$) and NiOOH-coated P-$BiVO_4$ (NiOOH-P-$BiVO_4$) [15]. The surface morphology of the as-prepared photoanodes was investigated by scanning electron microscopy. As shown in Fig. 1a, the bare $BiVO_4$ photoanode exhibits a nanoporous structure, in which $BiVO_4$ nanoparticles aggregate in the nanoplate structures, which is in agreement with the reported literature [6a]. The SEM image of P-$BiVO_4$ (Fig. 1b) reveals a highly similar structure, indicating that the post-synthetic treatment did not induce observable changes. Furthermore, the cocatalyst modification of bare $BiVO_4$ and P-$BiVO_4$ photoanodes also exhibits little changes in morphology (Fig. 1c and d), probably owing to the characteristic of loading amorphous thin layer as cocatalysts [15].

XRD patterns have been collected to explore the influence of the post-treatment as well as loading NiOOH on the crystal structure of the photoanodes. As can be seen in Fig. 1e, all the diffraction peaks are attributed to the crystal facets of monoclinic scheelite $BiVO_4$ (JCPDS no. 14–0688), except for the peaks annotated by asterisks which belong to the FTO substrate. The XRD patterns of these photoanodes are highly similar to each other due to the surface treatment and amorphous nature of the cocatalysts. Raman spectroscopy was then carried out to analyze possible structural changes induced by the post-treatment and the loading of NiOOH. As shown in Fig. 1f, the Raman bands located at 126, 211, 327, 367, 712, 827 $cm^{-1}$ are all from the typical vibration modes of $BiVO_4$ and no detectable changes in Raman shift can be observed among these photoanodes [18]. The features at 126 and 211 $cm^{-1}$ are attributed to the crystal vibration modes of $BiVO_4$. The bending modes of $VO_4$ tetrahedra correspond to the peaks at 327 and 367 $cm^{-1}$, while the shifts at 712 and 827 $cm^{-1}$ correspond to the antisymmetric and symmetric stretching vibration modes of the $VO_4$ tetrahedra, respectively [18c,19]. In addition, the UV–visible absorption spectra were examined to explore the light absorption properties of these photoanodes. As shown in Fig. 1g, the $BiVO_4$, P-$BiVO_4$, NiOOH-$BiVO_4$, and NiOOH-P-$BiVO_4$ photoanodes exhibit similar absorption edges at around 510 nm. Besides, the calculated Tauc plots indicate that these photoanodes have a similar bandgap of approximately 2.44 eV, which is in agreement with the previous literature [1a,3a]. The as-prepared semiconductors

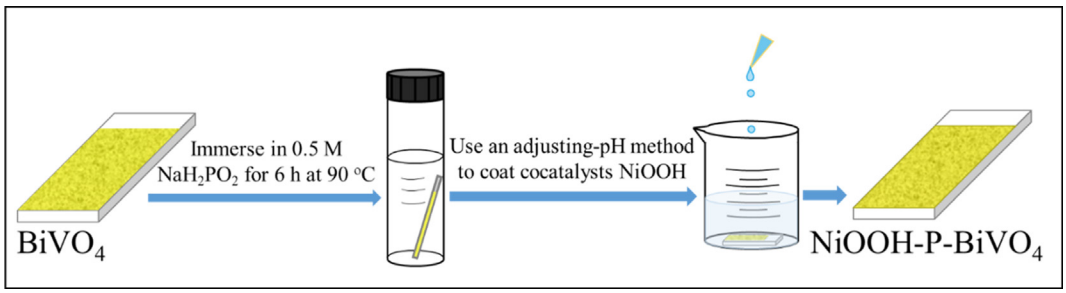


**Scheme 1.** Preparation of NiOOH-P-$BiVO_4$ photoanodes.

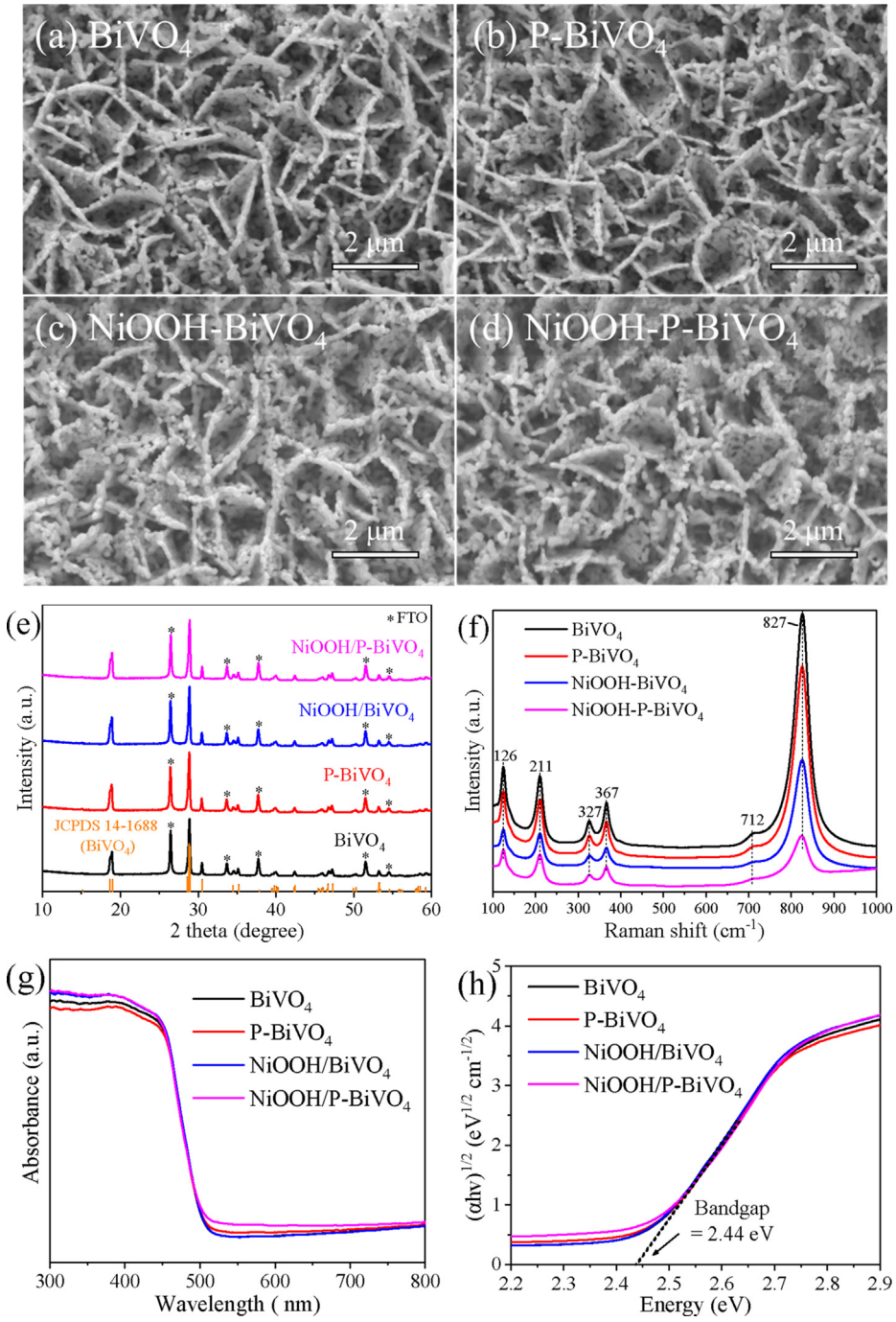


**Fig. 1.** SEM images of the (a) $BiVO_4$, (b) P-$BiVO_4$, (c) NiOOH-$BiVO_4$, and (d) NiOOH-P-$BiVO_4$ photoanodes, and (e) XRD patterns, (f) Raman spectra, (g) UV–visible absorption spectra and (h) calculated Tauc plots of these photoanodes.

still retained more than 95% of the initial absorption after 40 days of exposure. Due to the fact that SEM images, XRD patterns, Raman spectra, and UV–visible spectra exhibit no noticeable differences among the $BiVO_4$, P-$BiVO_4$, NiOOH-$BiVO_4$, and NiOOH-P-$BiVO_4$ photoanodes, we infer that the bulk physical properties remain unchanged after the post-treatment and the loading of NiOOH cocatalysts.

Therefore, efficacious techniques including transmission electron microscopy, X-ray photoelectron spectroscopy, and electron paramagnetic resonance spectroscopy, have been employed to explore the morphological and structural alternations at the surface of these photoanodes. As shown in Figure S2a-c, no difference can be observed between the TEM images of the $BiVO_4$ and P-$BiVO_4$ photoanodes, while the NiOOH-P-$BiVO_4$ photoanode possesses an amorphous floccus-like structure at its surface which should be the loaded NiOOH cocatalysts. Besides, the SAED patterns reveal the single-crystalline nature of the $BiVO_4$ nanoparticles (Figure S2-d-f). High-resolution TEM images were further collected, as presented in Fig. 2. The lattice spacings of the $BiVO_4$, P-$BiVO_4$, and NiOOH-P-$BiVO_4$ photoanodes were determined to be 0.46 nm, 0.31 nm, and 0.47 nm, which correspond to (011), (−121), and (011) planes, respectively. Fig. 2a indicates that the bare $BiVO_4$ photoanode has a relatively smooth surface. In contrast, it is worthy noted that a disordered atomic layer with a width of 2–3 nm has been created at the surface of the P-$BiVO_4$ photoanode (yellow dash in Fig. 2b), which is related to the improved charge transfer property in $BiVO_4$ [20]. The disordered surface layer can be preserved after further loading thin overlayer of NiOOH (yellow dash in Fig. 2c). Apart from this, the lattice spacing of 0.243 nm, corresponding to the (101) plane of nickel oxide hydroxide (JCPDS no. 06–0075), indicates that the formed cocatalysts are NiOOH instead of $Ni(OH)_2$ or NiO. We also present another clearer TEM image of the NiOOH-P-$BiVO_4$ photoanode in order to confirm the finding (Figure S3). The EDS spectrum reveals that surface elements are C, Cu, Bi, V, O, and Ni (Figure S4). The C signals may be induced by adventitious carbon contamination and the Cu signals are from the substrate, Cu mesh. Additionally, Fig. 2g shows the EDS mapping results of the NiOOH-P-$BiVO_4$ photoanode. Besides Bi, V and O, the element Ni can also be observed to uniformly exist at the surface of the photoanode. The weight and atomic proportion of the elements O, V, Ni, and Bi are listed in Table S2. Finally, it is explained that the semicircle structures shown in Fig. 2b (grey arrows) were induced by the electron-beam reduction process during TEM measurements.

To explore the surface chemical characteristic of these photoanodes, X-ray photoelectron spectroscopy technique was carried out. As shown in Figure S5, the XPS full survey spectra indicate the existence of Bi, V, and O in both $BiVO_4$ and P-$BiVO_4$ photoanodes. In addition to these elements, the signals of Ni have been detected in both NiOOH-$BiVO_4$ and NiOOH-P-$BiVO_4$ photoanodes. Fig. 3a shows the deconvoluted peaks for high-resolution O 1 s spectra of these photoanodes. The O 1 s spectra can be fitted into three

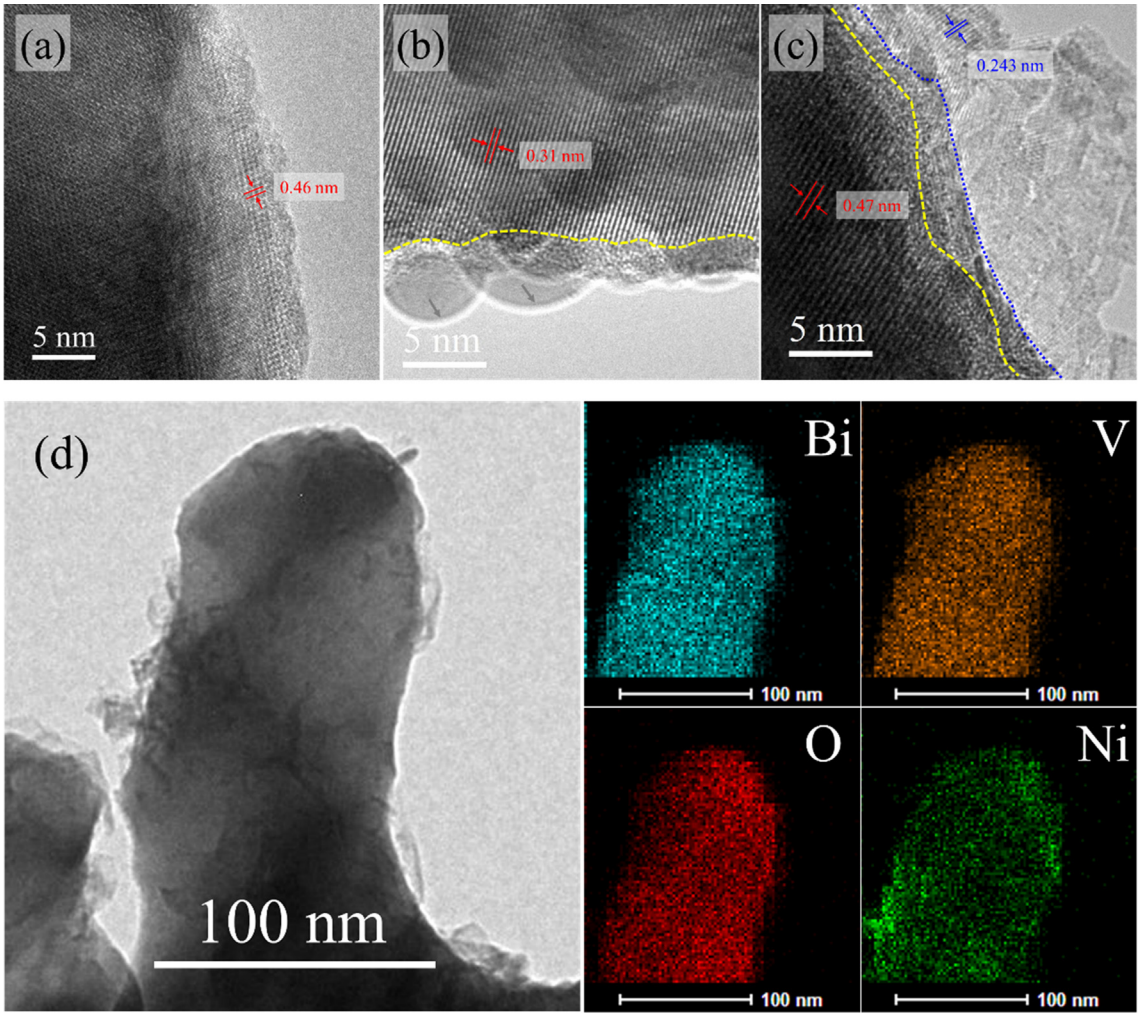


**Fig. 2.** High-resolution TEM images of the (a) $BiVO_4$, (b) P-$BiVO_4$, and (c) NiOOH-P-$BiVO_4$ photoanodes, and (d) EDS elemental mapping of the NiOOH-P-$BiVO_4$ photoanode.

peaks at 529.6 eV, 530.9 eV, and 531.8 eV, corresponding to lattice oxygen ($O_L$), oxygen vacancy ($O_{vac}$), and chemically absorbed oxygen ($O_C$), respectively [12,21]. The proportion of the peak areas is summarized in Table S1. It is noteworthy that the proportion of $O_{vac}$ increases to 22% in the P-$BiVO_4$ photoanode, 2-time higher than that of bare $BiVO_4$, demonstrating the successful introduction of $O_{vac}$ using the hypophosphite treatment [1e]. In addition to the XPS analysis, we also employed electron paramagnetic resonance (EPR) spectroscopy to verify the generation of $O_{vac}$. As shown in Figure S6, the P-$BiVO_4$ photoanode exhibits an apparent high EPR signal in comparison to the bare $BiVO_4$. The EPR signal at g = 2.00 can be attributed to the Zeeman effect of single-electron-trapped $O_{vac}$ [22]. The high signal of the P-$BiVO_4$ photoanode indicates an improved level of $O_{vac}$, in line with the results of O 1 s deconvolution. In addition to the $BiVO_4$ and P-$BiVO_4$ photoanodes, further overlaying NiOOH cocatalysts improves the amount of $O_{vac}$ to 30% in the NiOOH-P-$BiVO_4$ photoanode, compared to 26% in the NiOOH-$BiVO_4$.

The Bi 4f, V 2p, and Ni 2p high-resolution XPS spectra of these photoanodes have been examined as well (Fig. 3b-d). Compared with $BiVO_4$, the P-$BiVO_4$, NiOOH-$BiVO_4$, and NiOOH-P-$BiVO_4$ photoanodes exhibit obvious low-energy shifts of Bi 4f and V 2p (red dash in Fig. 3b-c), revealing that the metal elements have been partially reduced, probably from $Bi^{3+}$ to $Bi^{2+}$ and from $V^{5+}$ to $V^{4+}$ [23]. In addition to the existence of $Bi^{3+}$ ($4f_{7/2}$ and $4f_{5/2}$ peaks located at 158.9 eV and 164.2 eV), the deconvolution of Bi 4f spectra indicates that the P-$BiVO_4$, NiOOH-$BiVO_4$, and NiOOH-P-$BiVO_4$ photoanodes also exhibit two other species of $4f_{7/2}$ (158.1 eV) and $4f_{5/2}$ (163.4 eV), which may be attributed to $Bi^{2+}$ [1e,23c]. Similarly, the deconvoluting results of V 2p spectra also show the presence of $V^{4+}$ in the P-$BiVO_4$, NiOOH-$BiVO_4$, and NiOOH-P-$BiVO_4$ photoanodes (515.7 eV and 522.8 eV for $V^{4+}$ $2p_{3/2}$ and $V^{4+}$ $2p_{1/2}$, respectively), while all the photoanodes possess the peaks located at 516.5 eV and 524.1 eV, which are ascribed to $V^{5+}$ $2p_{3/2}$ and $V^{5+}$ $2p_{1/2}$ spin–orbit splits, respectively [1e,23c]. The Ni high-resolution spectra were also characterized

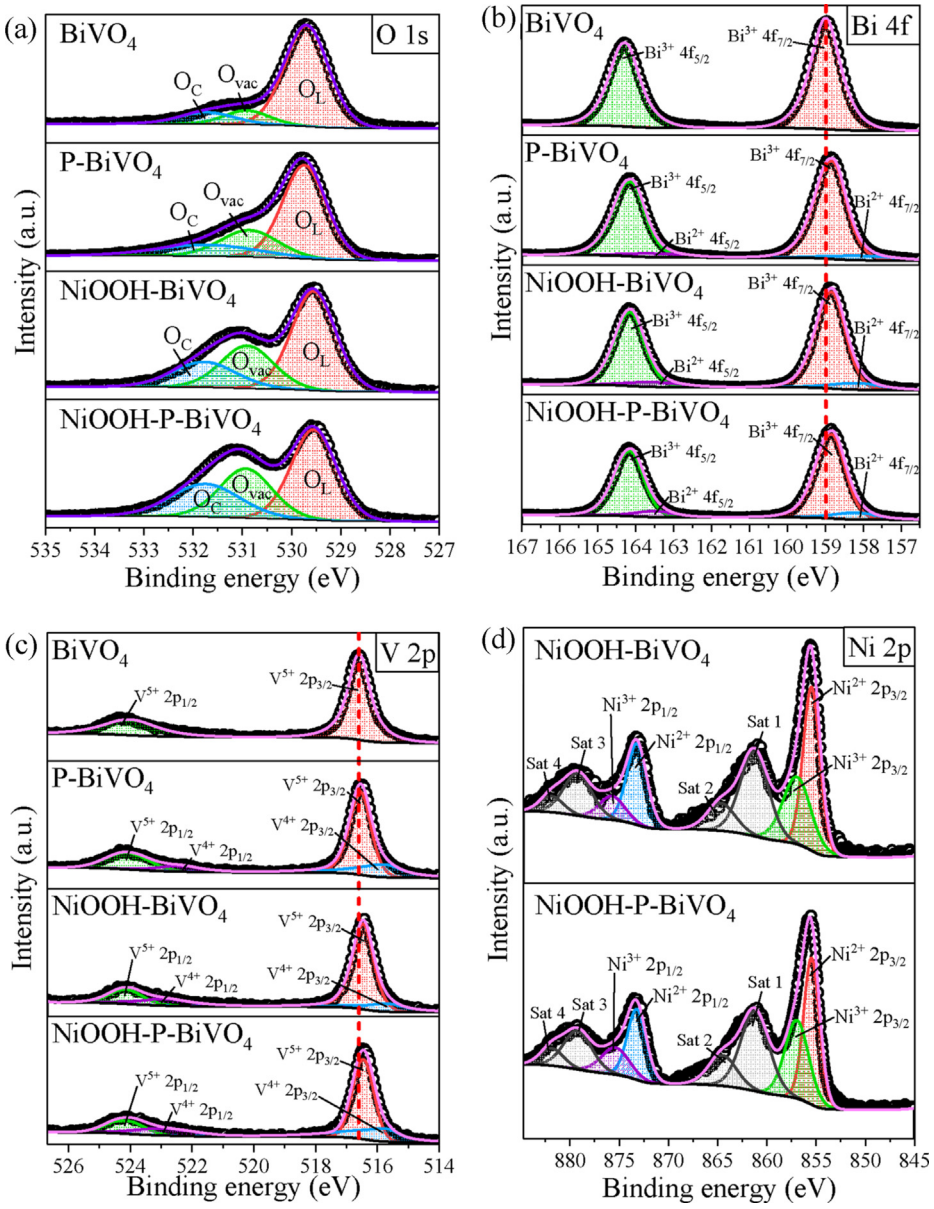


**Fig. 3.** High-resolution XPS spectra of (a) O 1 s, (b) Bi 4f, and (c) V 2p of the $BiVO_4$, P-$BiVO_4$, NiOOH-$BiVO_4$, NiOOH-P-$BiVO_4$ photoanodes, and (d) Ni 2p XPS spectra of the NiOOH-$BiVO_4$ and NiOOH-P-$BiVO_4$ photoanodes.

to prove the formation of NiOOH with the pH-adjusting method. As shown in Fig. 3d, the fitted peaks located at 855.5 eV ($Ni^{2+}$ $2p_{3/2}$), 856.0 eV ($Ni^{3+}$ $2p_{3/2}$), 873.2 eV ($Ni^{2+}$ $2p_{1/2}$), and 875.7 eV ($Ni^{3+}$ $2p_{1/2}$) illustrate the presence of $Ni^{2+}$ and $Ni^{3+}$, which is consistent with previous XPS results of $Ni(OH)_2$ and NiOOH [15,24]. The satellite peaks can also be fitted as Sat 1, 2, 3, and 4 in the XPS deconvolution spectra

To prove the effectiveness of sandwiching an $O_{vac}$ interlayer between the bulk $BiVO_4$ and the NiOOH overlayer, the photocurrent-potential (*J-V*) curves of the bare $BiVO_4$, P-$BiVO_4$, NiOOH-$BiVO_4$, and NiOOH-P-$BiVO_4$ photoanodes were conducted using a three-electrode configuration under AM 1.5G simulated sunlight (100 mW/$cm^2$). As shown in Fig. 4a, the bare $BiVO_4$ photoanode exhibits a low photocurrent density of 1.1 mA $cm^{-2}$ at 1.23 V vs. RHE, which is comparable with the values in previous studies [6a,25]. After the post-treatment, the P-$BiVO_4$ photoanode reaches an improved photocurrent of 2.1 mA $cm^{-2}$ at 1.23 V vs. RHE. By further coating NiOOH using the pH-adjusting method, a high photocurrent of 3.2 mA $cm^{-2}$ at 1.23 V vs. RHE in the NiOOH-P-$BiVO_4$ photoanode is obtained, in comparison to 2.3 mA $cm^{-2}$ in the NiOOH-$BiVO_4$. The onset potential of both $BiVO_4$ and P-$BiVO_4$ photoanodes reduces from around 0.80 V vs. RHE to 0.54 V vs. RHE. In addition to the *J-V* measurements, transient amperometric measurements of these photoanodes were carried out at 1.23 V vs. RHE under chopped illumination to evaluate charge recombination rate at the electrode||electrolyte junction (Fig. 4b). Among these photoanodes, the $BiVO_4$ photoanode exhibits the sharpest photocurrent spike at the moment of light switch-on, indicating a considerable amount of charge carrier recombination. [26] After the hypophosphite treatment, the P-$BiVO_4$ photoanode displays smaller spikes, suggesting the alleviation of charge carrier recombination. Moreover, the subsequent loading of NiOOH on both $BiVO_4$ and P-$BiVO_4$ photoanodes further reduces the probability of charge recombination by accelerating surface hole transfer [27]. The dark currents of as-synthesized semiconductors were almost no change after 10 days. The degradations of PEC performance for those semiconductors were much slower (<5%) for the films stored under 0% RH and 50% RH after 35 days of exposure. In addition, the applied bias photon-to-current efficiency (ABPE), derived from the *J-V* curves [12], has been employed to evaluate the PEC efficiency of these modified $BiVO_4$ photoanodes. As shown in Fig. 4c, the bare $BiVO_4$ photoanode exhibits a maximum ABPE value of 0.12% at 1.00 V, while an improved efficiency of 0.21% at 1.01 V for the P-$BiVO_4$ photoanode is displayed. After loading NiOOH, the maximum ABPE values reach 0.43% and 0.66% at 0.88 V vs. RHE for NiOOH-$BiVO_4$ and NiOOH-P-$BiVO_4$ photoanodes, respectively. To further investigate the photoresponsive properties of NiOOH-P-$BiVO_4$ photoanode, incident photon-to-current conversion efficiency (IPCE) as a function of the wavelength of monochromatic light was performed at 1.23 V vs. RHE (Fig. 4d). The IPCE values of the NiOOH-P-$BiVO_4$ photoanode are 2.5–3.7 times higher than that of the bare $BiVO_4$, confirming the effectiveness of $O_{vac}$ as an interlayer between bulk $BiVO_4$ and overlayer NiOOH.

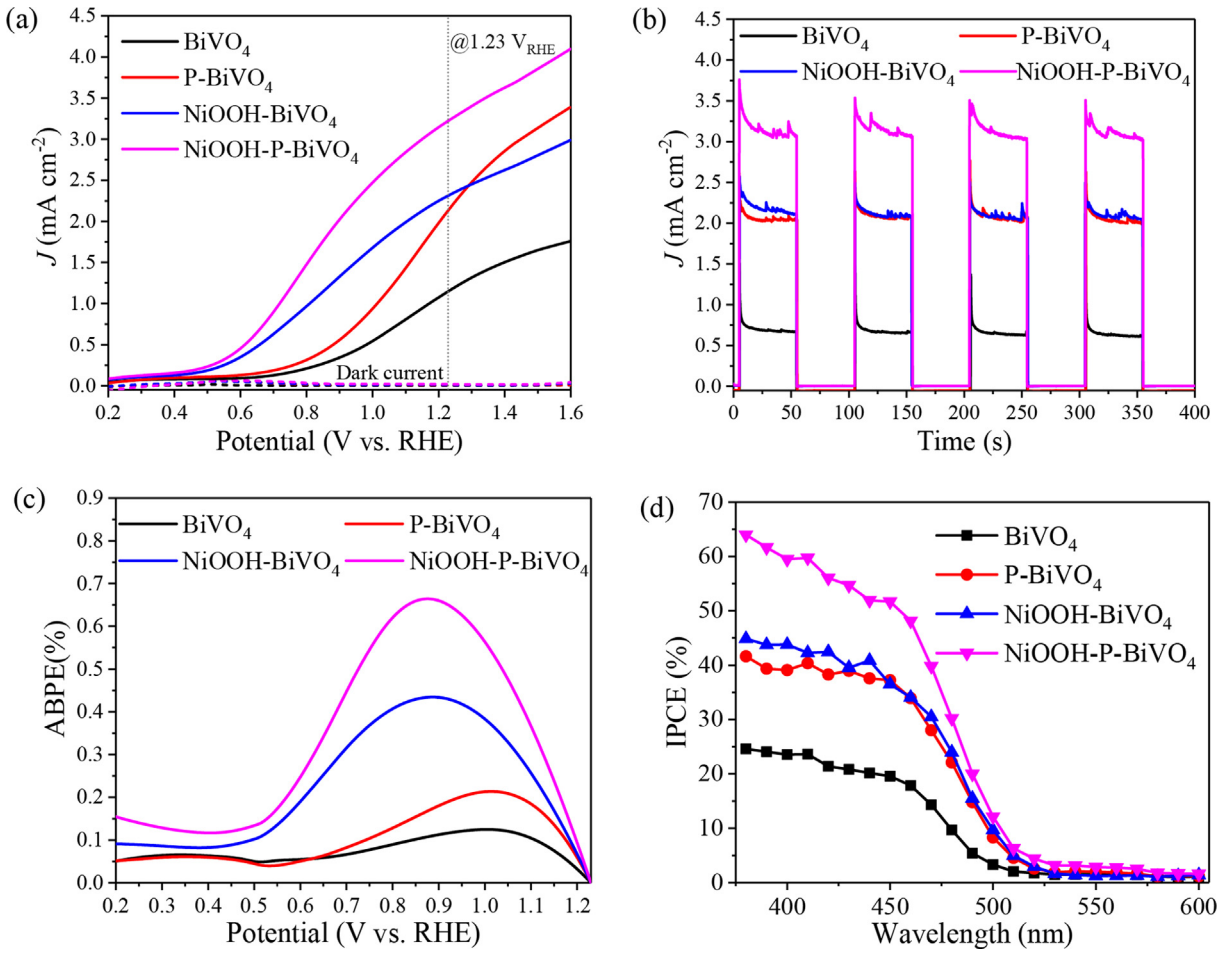


**Fig. 4.** (a) Photocurrent-potential (*J-V*) curves, (b) transient photocurrent response, (c) applied bias photon-to-current efficiency (ABPE), and (d) incident photon-to-current conversion efficiency (IPCE) of the $BiVO_4$, P-$BiVO_4$, NiOOH-$BiVO_4$, and NiOOH-P-$BiVO_4$ photoanodes.

To further demonstrate the effectiveness of the additional $O_{vac}$ interlayer, a 0.5 M sodium sulfite aqueous solution as hole scavenger was used as an electrolyte for the *J-V* measurements. As shown in Figure S7a, all the photoanodes exhibit improved photocurrents when measuring in the hole scavenger solution. It is noteworthy that the NiOOH-$BiVO_4$ photoanode has a decreased photocurrent density of 4.42 mA $cm^{-2}$ at 1.23 V vs. RHE, in comparison to 4.78 mA $cm^{-2}$ in the bare $BiVO_4$ photoanode, which may be due to the recombination of electron-hole pairs at the $BiVO_4$||NiOOH interface [6a,28]. By contrast, the P-$BiVO_4$ photoanode exhibits the highest photocurrent density of 4.98 mA $cm^{-2}$ at 1.23 V vs. RHE, which may be attributed to the suppressed charge carrier recombination as a result of the surface $O_{vac}$ interlayer. Because of the alleviated interfacial charge recombination, the photoresponse of the NiOOH-P-$BiVO_4$ photoanode reaches 4.85 mA $cm^{-2}$ at 1.23 V vs. RHE, compared to 4.42 mA $cm^{-2}$ of the NiOOH-$BiVO_4$. The cumulative photocurrent densities ($J_{absorption}$) of these photoanodes were also collected. As shown in Figure S7b, the bare $BiVO_4$, P-$BiVO_4$, NiOOH-$BiVO_4$, and NiOOH-P-$BiVO_4$ photoanodes exhibit theoretical photocurrents of 5.53, 5.55, 5.58, and 5.60 mA $cm^{-2}$, respectively, suggesting that all absorbed light energy is mostly converted into chemical energy.

Based on experimental data, the charge separation ($\eta_{separtion}$) and charge transfer ($\eta_{transfer}$) efficiencies have been evaluated. As shown in Fig. 5a, the resulting charge separation efficiency decreases from 86% in the $BiVO_4$ to 77% in the NiOOH-$BiVO_4$ photoanode at 1.23 V vs. RHE, revealing the occurrence of interfacial charge recombination at the $BiVO_4$||NiOOH interface [6a,28]. The introduction of the $O_{vac}$ interlayer prior to loading NiOOH clearly enhances the charge separation efficiency from 77% in the NiOOH-$BiVO_4$ to 85% in the NiOOH-P-$BiVO_4$ photoanode. Moreover, surface hole transfer efficiency can also be enhanced with the post-treatment as well as the loading of NiOOH (Fig. 5b).

Electrochemical impedance spectroscopy was further implemented to explore the surface charge transfer properties of these photoanodes [3a,5c]. The resultant EIS data were fitted with respect to the equivalent circuit model inserted in Fig. 5c, and fitting parameters are shown in Table S3. In comparison to bare $BiVO_4$, the reduced charge transfer resistance ($R_{ct}$) in the P-$BiVO_4$ and NiOOH-$BiVO_4$ photoanodes indicates enhanced surface hole transfer. Interestingly, the NiOOH-P-$BiVO_4$ photoanode exhibits an $R_{ct}$ of 795 Ω between that of P-$BiVO_4$ (681 Ω) and NiOOH-$BiVO_4$ (954 Ω), implying that the $O_{vac}$ interlayer might not be completely wrapped by the NiOOH overlayer, which is in agreement with the TEM observation. Moreover, the Mott-Schottky measurements were performed to estimate the charge carrier density in these photoanodes [1e,3b]. As shown in Fig. 5d, all the photoanodes exhibit positive slopes, revealing the *n*-type semiconductor nature of the materials. The calculated donor densities are $4.91 \times 10^{-26}$, $1.16 \times 10^{-25}$, $4.95 \times 10^{-26}$, and $9.72 \times 10^{-26}$ $m^{-3}$ for the $BiVO_4$, P-$BiVO_4$, NiOOH-$BiVO_4$, and NiOOH-P-$BiVO_4$ photoanodes, respectively. It is evident that the donor density can be improved with the hypophosphite treatment but not the loading of NiOOH. The increased charge carrier density in the P-$BiVO_4$ photoanode is probably due to the suppressed carrier recombination [1e]. The charge carrier recombination in these photoanodes has been evaluated by photoluminescence (PL) emission spectra and time-resolved photoluminescence (TRPL) decay [29]. As shown in Figure S8a, all the photoanodes exhibit emission peaks at around 510 nm. The peak intensity decreases after the hypophosphite treatment and the loading of NiOOH, suggesting an overall suppression of charge recombination [29]. The TRPL technique was further utilized to explore the charge transport behavior in these

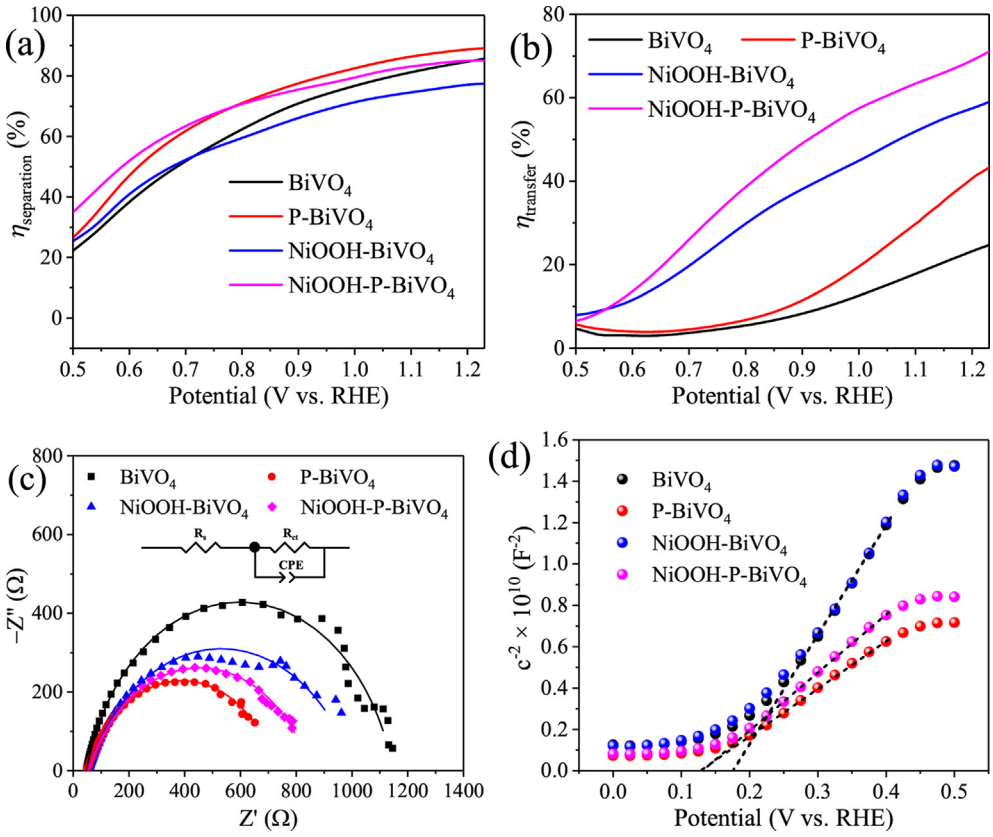


**Fig. 5.** (a) Charge separation efficiency ($\eta_{separtion}$), (b) charge transfer efficiency ($\eta_{transfer}$), (c) electrochemical impedance spectra (EIS), and (d) Mott-Schottky (M−S) plots of the $BiVO_4$, P-$BiVO_4$, NiOOH-$BiVO_4$, and NiOOH-P-$BiVO_4$ photoanodes.

photoanodes. The resultant TRPL curves were fitted using a tri-exponential decay function to estimate charge carrier lifetime (Figure S8b). As shown in Table S4, compared to bare $BiVO_4$ (9.02 ns), the increased average lifetimes in the P-$BiVO_4$ (10.58 ns), NiOOH-$BiVO_4$ (14.09 ns) and NiOOH-P-$BiVO_4$ (14.84 ns), clearly indicates the reduced charge recombination rates.

The chemical stability of the $O_{vac}$ in photoelectrodes is of significance during the practical water splitting process. However, the stability mainly depends upon the processing approaches. For example, a previous study shows that argon-plasma-implantation generated $O_{vac}$ has high stability over 40 h, owing to the increased active sites as well as optimized absorption and activation of water molecules [30]. By contrast, the argon-annealing process can also induce $O_{vac}$, but the $O_{vac}$-rich $BiVO_4$ photoanode exhibits inferior stability, and the photocurrent density decreases from 1.1 mA $cm^{-2}$ to 0.6 mA $cm^{-2}$ [12]. In this work, 5-h amperometric measurements were carried out to evaluate the stability of the bare $BiVO_4$, P-$BiVO_4$, NiOOH-$BiVO_4$, and the NiOOH-P-$BiVO_4$ photoanodes. As shown in Figure S9, the bare $BiVO_4$ photoanode exhibits a rapidly decreased photocurrent from 0.7 mA $cm^{-2}$ to 0.2 mA $cm^{-2}$, revealing the photocorrsion of the $BiVO_4$ photoanodes [2e,23c]. With the post-treatment, the photocurrent density of the P-$BiVO_4$ decreases from 1.8 mA $cm^{-2}$ to 0.5 mA $cm^{-2}$, indicating the induced $O_{vac}$ may not be stable during the water oxidation process. After loading a NiOOH layer, the stability of the NiOOH-P-BiVO4 photoanode exhibits a substantial improvement, from 3.2 mA $cm^{-2}$ to 2.0 mA $cm^{-2}$ during the process. The decreased photocurrent density may be due to the dropping of the amorphous floccus-like structure of the NiOOH layer during the 5-h tests [31]. Thus, further study on loading a uniform and thin layer as cocatalysts while preserving the generated $O_{vac}$ layer may contribute to the performance and the stability of various photoelectrodes [12].

$O_{vac}$ can be generated by a number of approaches including plasma/ion implantation [30,32], hydrogenation [33], post-annealing under inert atmosphere (e.g. Ar and $N_2$) [34], reaction with reducing reagents [20a,c], electrochemical treatment [23], and elemental doping [35]. An inexpensive, effective, and facial hypophosphite treatment to induce $O_{vac}$ in the $BiVO_4$ photoanodes is presented in this work. The treatment alters the surface structure of these photoanodes but has little influence on the bulk characteristics, probably owing to the mild reduction activity of the chemical. It is reported that intrinsic $O_{vac}$ can function to enhance charge mobility since two electrons released with the formation of one oxygen vacancy [36], which could be the reason for the enhanced charge carrier density, as indicated by the M−S measurement. Besides, the introduction of $O_{vac}$ may tune the electronic structure of the $BiVO_4$ photoanode, possibly resulting in the formation of an inter-band state [1e]. Such inter-band state has the chance to combine with the NiOOH overlayer to create a Helmholtz layer potential drop, which might be responsible for the suppression of interfacial recombination at the $BiVO_4$||NiOOH junction [6a]. The charge transfer property of the P-$BiVO_4$ is enhanced in comparison to the bare $BiVO_4$, suggesting that the generated $O_{vac}$ might directly participate in the water oxidation reaction [23c,30]. Despite this, the hypophosphite-induced $O_{vac}$ did not lower the onset potential of the *J-V* curves. Further exploration on the structural and electronic structure of $O_{vac}$ is of critical importance to determine how the $O_{vac}$, as surface states, to tune the energy level as well as to participating in the surface water oxidation reaction.

## 4. Conclusion

In summary, a chemical treatment method has been utilized to create an $O_{vac}$ interlayer at the surface of $BiVO_4$ photoanode. The generated $O_{vac}$ interlayer, sandwiched between the bulk $BiVO_4$ and an OECNiOOH overlayer, can function to reduce interfacial charge recombination. Thereby, the rational construction of the BiVO4/$O_{vac}$/NiOOH structure improves charge separation and charge transport efficiencies, giving rise to the enhanced performance of PEC water oxidation. In addition, the chemical stability of the NiOOH-coated hypophosphite-treated $BiVO_4$ photoanode is also improved, probably resulting from the reduced photocorrosion in the photoanode. The NiOOH cocatalyst can prevent the decrement of $O_{vac}$, while the $O_{vac}$ interlayer serves as an inter-band state to reduce charge-carrier recombination. This work demonstrates effective coordination between $O_{vac}$ and cocatalysts, which paves a new route to develop efficient photo-responsive materials for practical applications in the field of PEC water splitting.

## Declaration of Competing Interest

The authors declare that they have no known competing financial interests or personal relationships that could have appeared to influence the work reported in this paper.

## Acknowledgements

The authors acknowledge financial support from the Research Grants Council of Hong Kong (grant no. 21203518, F-CityU106/18 and 9048121), City University of Hong Kong (grant no. 9667229, 7005289, 7005580, 7005720, 9680208, 9667213 and 9052029), Shenzhen Science Technology and Innovation Commission (grant no. R-IND12302) as well as National Natural Science Foundation of China (grant no. 22071070, 21974131 51701159, 52022054, and 51974181).

## Appendix A. Supplementary data

Supplementary data to this article can be found online at https://doi.org/10.1016/j.jcis.2021.10.063.

## References

[1] a Q. Meng, B. Zhang, L. Fan, H. Liu, M. Valvo, K. Edström, M. Cuartero, R. de Marco, G. A. Crespo, L. Sun, *Angew. Chem. Int. Ed.* **2019**, *58*, 19027-19033; b J. H. Kim, J. S. Lee, *Adv. Mater.* **2019**, *31*, 1970146; c C. H. Mak, X. Han, M. Du, J.-J. Kai, K. F. Tsang, G. Jia, K.-C. Cheng, H.-H. Shen, H.-Y. Hsu, *Journal of Materials Chemistry A* **2021**, *9*, 4454-4504; d P. Luan, J. Zhang, *ChemElectroChem* **2019**, *6*, 3227-3243; e S. Feng, T. Wang, B. Liu, C. Hu, L. Li, Z. J. Zhao, J. Gong, *Angew. Chem. Int. Ed.* **2020**, *59*, 2044-2048.

[2] a F. S. Hegner, I. Herraiz-Cardona, D. Cardenas-Morcoso, N. r. López, J.-R. n. Galán-Mascarós, S. Gimenez, *ACS Appl. Mater. Interfaces* **2017**, *9*, 37671-37681; b Y. Lu, J. Su, J. Shi, D. Zhou, *ACS Appl. Energy Mater.* **2020**, *3*, 9089-9097; c R. Liu, C. H. Mak, X. Han, Y. Tang, G. Jia, K.-C. Cheng, H. Qi, X. Zou, G. Zou, H.-Y. Hsu, *Journal of Materials Chemistry A* **2020**, *8*, 23803-23811; d H.-Y. Hsu, L. Ji, C. Zhang, C. H. Mak, R. Liu, T. Wang, X. Zou, S.-Y. Leu, E. T. Yu, *Journal of Materials Chemistry C* **2018**, *6*, 11552-11560; e H. Sun, W. Hua, Y. Li, J.-G. Wang, *ACS Sustain. Chem. Eng.* **2020**, *8*, 12637-12645.

[3] a X. Yin, W. Qiu, W. Li, C. Li, K. Wang, X. Yang, L. Du, Y. Liu, J. Li, *Chem. Eng. J.* **2020**, *389*, 124365; b G. Liu, F. Li, Y. Zhu, J. Li, L. Sun, *RSC Adv.* **2020**, *10*, 28523-28526.

[4] a Y. Qiu, W. Liu, W. Chen, G. Zhou, P.-C. Hsu, R. Zhang, Z. Liang, S. Fan, Y. Zhang, Y. Cui, *Sci. Adv.* **2016**, *2*, e1501764; b C. H. Mak, R. Liu, X. Han, Y. Tang, X. Zou, H. H. Shen, Y. Meng, G. Zou, H. Y. Hsu, *Advanced Optical Materials* **2020**, *8*, 2001023; c C. H. Mak, X. Huang, R. Liu, Y. Tang, X. Han, L. Ji, X. Zou, G. Zou, H.-Y. Hsu, *Nano Energy* **2020**, 104752.

[5] a Q. Pan, C. Zhang, Y. Xiong, Q. Mi, D. Li, L. Zou, Q. Huang, Z. Zou, H. Yang, *ACS Sustain. Chem. Eng.* **2018**, *6*, 6378-6387; b Y. Tang, C. H. Mak, R. Liu, Z. Wang, L. Ji, H. Song, C. Tan, F. Barrière, H. Y. Hsu, *Advanced Functional Materials* **2020**, 2006919; c S. Xu, D. Fu, K. Song, L. Wang, Z. Yang, W. Yang, H. Hou, *Chem. Eng. J.* **2018**, *349*, 368-375.

[6] a T. W. Kim, K.-S. Choi, *Science* **2014**, *343*, 990-994; b R. Yalavarthi, R. Zbořil, P. Schmuki, A. Naldoni, Š. Kment, *J. Power Sources* **2021**, *483*, 229080.

[7] G. Ai, R. Mo, H. Li, J. Zhong, Nanoscale 7 (2015) 6722–6728.

[8] J.H. Kim, S. Han, Y.H. Jo, Y. Bak, J.S. Lee, J. Mater. Chem. A 6 (2018) 1266–1274.

[9] a R. Li, H. Han, F. Zhang, D. Wang, C. Li, *Energy Environ. Sci.* **2014**, *7*, 1369-1376; b T.-H. Lai, I. Constantinou, C. M. Grand, E. D. Klump, S. Baek, H.-Y. Hsu, S.-W. Tsang, K. S. Schanze, J. R. Reynolds, F. So, *Chemistry of Materials* **2016**, *28*, 2433-2440; c Z. Wang, G. Liu, C. Ding, Z. Chen, F. Zhang, J. Shi, C. Li, *J. Phys. Chem. C* **2015**, *119*, 19607-19612.

[10] a J. Quiñonero, R. Gómez, *Appl. Catal. B* **2017**, *217*, 437-447; b G. Wang, Y. Ling, X. Lu, T. Zhai, F. Qian, Y. Tong, Y. Li, *Nanoscale* **2013**, *5*, 4129-4133; c H. Lim, J. Y. Kim, E. J. Evans, A. Rai, J.-H. Kim, B. R. Wygant, C. B. Mullins, *ACS Appl. Mater. Interfaces* **2017**, *9*, 30654-30661; d S. Yoon, J.-H. Lim, B. Yoo, *Electrochim. Acta* **2017**, *237*, 37-43; e H. She, P. Yue, J. Huang, L. Wang, Q. Wang, *Chem. Eng. J.* **2020**, *392*, 123703; f P. Yue, H. She, L. Zhang, B. Niu, R. Lian, J. Huang, L. Wang, Q. Wang, *Appl. Catal. B* **2021**, *286*, 119875; g S. Zhou, K. Chen, J. Huang, L. Wang, M. Zhang, B. Bai, H. Liu, Q. Wang, *Appl. Catal. B* **2020**, *266*, 118513.

[11] a Y. Li, L. Hu, W. Zheng, X. Peng, M. Liu, P. K. Chu, L. Y. S. Lee, *Nano Energy* **2018**, *52*, 360-368; b C. Dong, Y. Wang, H. Wang, C. S. K. Lin, H.-Y. Hsu, S.-Y. Leu, *Energy Procedia* **2019**, *158*, 918-925; c W. Guo, D. Li, D. Zhong, S. Chen, G. Hao, G. Liu, J. Li, Q. Zhao, *Nanoscale* **2020**, *12*, 983-990.

[12] J.B. Pan, B.H. Wang, J.B. Wang, H.Z. Ding, W. Zhou, X. Liu, J.R. Zhang, S. Shen, J.K. Guo, L. Chen, Angew. Chem. Int. Ed. 60 (2021) 1433–1440.

[13] a H.-Y. Hsu, H.-H. Hsieh, H.-Y. Tuan, J.-L. Hwang, *Solar energy materials and solar cells* **2010**, *94*, 955-959; b S. Rao, X. Zou, S. Wang, T. Shi, Y. Lu, L. Ji, H.-Y. Hsu, Q. Xu, X. Lu, *Journal of The Electrochemical Society* **2019**, *166*, D427; c Z. Tian, P. Zhang, P. Qin, D. Sun, S. Zhang, X. Guo, W. Zhao, D. Zhao, F. Huang, *Adv. Energy Mater.* **2019**, *9*, 1901287.

[14] a G. V. Govindaraju, G. P. Wheeler, D. Lee, K.-S. Choi, *Chem. Mater.* **2017**, *29*, 355-370; b X. Zou, L. Ji, H.-Y. Hsu, K. Zheng, Z. Pang, X. Lu, *Journal of Materials Chemistry A* **2018**, *6*, 12724-12732.

[15] B. Zhang, X. Huang, Y. Zhang, G. Lu, L. Chou, Y. Bi, Angew. Chem. Int. Ed. 59 (2020) 18990–18995.

[16] Y. Ma, S.R. Pendlebury, A. Reynal, F. Le Formal, J.R. Durrant, Chem. Sci. 5 (2014) 2964–2973.

[17] B.J. Trześniewski, I.A. Digdaya, T. Nagaki, S. Ravishankar, I. Herraiz-Cardona, D. A. Vermaas, A. Longo, S. Gimenez, W.A. Smith, Energy Environ. Sci. 10 (2017) 1517–1529.

[18] a J.-M. Wu, Y. Chen, L. Pan, P. Wang, Y. Cui, D. Kong, L. Wang, X. Zhang, J.-J. Zou, *Appl. Catal. B* **2018**, *221*, 187-195; b H.-Y. Hsu, L. Ji, M. Du, J. Zhao, T. Y. Edward, A. J. Bard, *Electrochimica Acta* **2016**, *220*, 205-210; c Y. Hermans, A. Klein, K. Ellmer, R. van de Krol, T. Toupance, W. Jaegermann, *J. Phys. Chem. C* **2018**, *122*, 20861-20870.

[19] a I. Constantinou, T. H. Lai, H. Y. Hsu, S. H. Cheung, E. D. Klump, K. S. Schanze, S. K. So, F. So, *Advanced Electronic Materials* **2015**, *1*, 1500167; b Y. Liang, T. Tsubota, L. P. A. Mooij, R. van de Krol, *J. Phys. Chem. C* **2011**, *115*, 17594-17598.

[20] a J. K. Kim, Y. Cho, M. J. Jeong, B. Levy-Wendt, D. Shin, Y. Yi, D. H. Wang, X. Zheng, J. H. Park, *ChemSusChem* **2018**, *11*, 933-940; b Z. Chen, H.-Y. Hsu, M. Arca, K. S. Schanze, *The Journal of Physical Chemistry B* **2014**, *119*, 7198-7209; cY. Peng, H. Wu, M. Yuan, F.-F. Li, X. Zou, Y. H. Ng, H.-Y. Hsu, *Sustain. Energy Fuels* **2021**, *10.1039/D0SE01901A*.

[21] P. Guan, H. Bai, F. Wang, H. Yu, D. Xu, W. Fan, W. Shi, Chem. Eng. J. 358 (2019) 658–665.

[22] J. Li, L. Guo, N. Lei, Q. Song, Z. Liang, ChemElectroChem 4 (2017) 2852–2861.

[23] a S. Wang, P. Chen, J. H. Yun, Y. Hu, L. Wang, *Angew. Chem. Int. Ed.* **2017**, *56*, 8500-8504; b J. Zhao, H. Yin, T. Lim, H. Xie, H.-Y. Hsu, F. Forouzan, A. J. Bard, *Journal of The Electrochemical Society* **2016**, *163*, D506-D514; c X. Yin, J. Li, L. Du, F. Zhan, K. Kawashima, W. Li, W. Qiu, Y. Liu, X. Yang, K. Wang, Y. Ning, C. B. Mullins, *ACS Appl. Energy Mater.* **2020**, *3*, 4403-4410.

[24] a N. Weidler, J. Schuch, F. Knaus, P. Stenner, S. Hoch, A. Maljusch, R. Schäfer, B. Kaiser, W. Jaegermann, *J. Phys. Chem. C* **2017**, *121*, 6455-6463; b A. P. Grosvenor, M. C. Biesinger, R. S. C. Smart, N. S. McIntyre, *Surf. Sci.* **2006**, *600*, 1771-1779.

[25] J. Qi, D. Kong, D. Liu, L. Pan, Y. Chen, X. Zhang, J.-J. Zou, RSC adv. 9 (2019) 15629–15634.

[26] F. Feng, C. Li, J. Jian, X. Qiao, H. Wang, L. Jia, Chemical Engineering Journal 368 (2019) 959–967.

[27] F. Tang, W. Cheng, H. Su, X. Zhao, Q. Liu, A.C.S. Appl, Mater. Interfaces 10 (2018) 6228–6234.

[28] H. He, A. Liao, W. Guo, W. Luo, Y. Zhou, Z. Zou, Nano Today 28 (2019) 100763.

[29] H.L. Tan, X. Wen, R. Amal, Y.H. Ng, J. Phys. Chem. Lett. 7 (2016) 1400–1405.

[30] S. Jin, X. Ma, J. Pan, C. Zhu, S.E. Saji, J. Hu, X. Xu, L. Sun, Z. Yin, Appl. Catal. B 281 (2021) 119477.

[31] a J. H. Kim, Y. Jo, J. H. Kim, J. W. Jang, H. J. Kang, Y. H. Lee, D. S. Kim, Y. Jun, J. S. Lee, *ACS nano* **2015**, *9*, 11820-11829; b Y. Shi, Y. Yu, Y. Yu, Y. Huang, B. Zhao, B. Zhang, *ACS Energy Letters* **2018**, *3*, 1648-1654.

[32] N. Liu, V. Häublein, X. Zhou, U. Venkatesan, M. Hartmann, M. Mačković, T. Nakajima, E. Spiecker, A. Osvet, L. Frey, P. Schmuki, *Nano lett.* **2015**, *15*, 6815-6820.

[33] N. Liu, C. Schneider, D. Freitag, M. Hartmann, U. Venkatesan, J. Müller, E. Spiecker, P. Schmuki, Nano lett. 14 (2014) 3309–3313.

[34] a Y. Chen, M. Yang, J. Du, G. Ke, X. Zhong, Y. Zhou, F. Dong, L. Bian, H. He, *J. Mater. Sci.* **2019**, *54*, 671-682; b T. W. Kim, Y. Ping, G. A. Galli, K.-S. Choi, *Nat. Commun.* **2015**, *6*, 1-10.

[35] Q. Pan, K. Yang, G. Wang, D. Li, J. Sun, B. Yang, Z. Zou, W. Hu, K. Wen, H. Yang, Chem. Eng. J. 372 (2019) 399–407.

[36] H. Seo, Y. Ping, G. Galli, Chem. Mater. 30 (2018) 7793–7802.